scientific reports

Check for updates

OPEN

Single-cell mitochondrial morphomics reveals cellular heterogeneity and predicts complex I, III, and ATP synthase Inhibition responses

Ratneswary Sutharsan[1,2], Maddi Biaut Hontaas[1,7], Yan Li[1,2,7], Hao Xiong[1,3,7], Hartwig Preckel[4], Carolyn M. Sue[1,6] & Gautam Wali[1,2,5]✉

Mitochondrial heterogeneity drives diverse cellular responses in neurodegenerative diseases, complicating the evaluation of mitochondrial dysfunction. In this study, we describe a high-throughput imaging and analysis approach to investigate cell-to-cell mitochondrial variability. We applied known mitochondrial function inhibitors - rotenone, antimycin, and oligomycin to inhibit complexes I, III, and V (ATP synthase) function in human induced pluripotent stem cell-derived cortical neurons, a model commonly used in neurodegenerative disease research. We captured a large number of cell images and extracted a diverse range of mitochondrial morphological features related to shape, size, texture, and spatial distribution, for an unbiased and comprehensive analysis of mitochondrial morphology. Group-level cell analysis, which examines the collective responses of cells exposed to the same mitochondrial inhibitor, showed that cells treated with rotenone, antimycin, or oligomycin clustered together based on their shared morphological changes. Rotenone and antimycin, both targeting different complexes of the electron transport chain, formed sub-clusters within a larger cluster. In contrast, oligomycin, which inhibits ATP synthase, resulted in a distinct cluster likely due to its differing effect on ATP production. Single-cell analysis using dimensionality reduction techniques revealed distinct subpopulations of cells with varying degrees of sensitivity to each mitochondrial inhibitor, identifying the most affected cells. Mitochondrial feature differential expression analysis showed that neurite-related mitochondrial features, such as intensity and size, were more severely impacted than cell body-related mitochondrial features, particularly with rotenone and antimycin, which target the electron transport chain. In contrast, oligomycin which affects ATP synthesis by directly inhibiting ATP synthase showed relatively less severe alterations in neurite-related mitochondrial features, highlighting a distinct effect of the mode of action between inhibitors. By incorporating the most affected cells into machine learning models, we significantly improved the prediction accuracy of mitochondrial dysfunction outcomes – 81.97% for antimycin, 75.12% for rotenone, and 94.42% for oligomycin. This enhancement underscores the value of targeting highly responsive cell subpopulations, offering a more precise method for evaluating mitochondrial modulators and therapeutic interventions in neurodegenerative diseases.

In neurodegenerative diseases, mitochondrial dysfunction can result from genetic predispositions and/or environmental factors, such as toxins and pollutants, triggering a cascade of downstream events, eventuating in neuronal dysfunction or degeneration, thereby leading to clinical phenotypes[1]. Mitochondria in neurons are involved in a range of cellular functions essential for maintaining neuronal activity and survival, including adenosine triphosphate (ATP) synthesis, axonal transport, synaptic function and plasticity, reactive oxygen

[1]Neuroscience Research Australia (NeuRA), Sydney, Australia. [2]School of Biomedical Sciences, University of New South Wales, Sydney, Australia. [3]Centre for Health Informatics, Macquarie University, Sydney, Australia. [4]Revvity Cellular Technologies GmbH, Hamburg, Germany. [5]Neuroscience Research Australia (NeuRA), Margarete Ainsworth Building, 139, Barker St, Randwick, NSW 2031, Australia. [6] School of Clinical Medicine, University of New South Wales, Sydney, Australia. [7]Maddi Biaut Hontaas, Yan Li and Hao Xiong contributed equally to this work. ✉email: g.wali@unsw.edu.au

species (ROS) management, calcium homeostasis, and the regulation of apoptosis[2,3]. To carry out these processes, mitochondria continuously undergo various structural modifications through processes such as - fusion and fission, cristae remodelling, motility, mitophagy, and their interaction with other organelles[4–6], ensuring cellular homeostasis in response to physiological or environmental stimuli[4,7]. Mitochondrial morphology is strongly linked to its pathology and morphology-based assays evaluating mitochondrial size and interconnectivity using morphological features such as mitochondrial area, form factor, and aspect ratio are commonly used as indicators of mitochondrial health. For example, inhibition of complex I in human fibroblasts reduced mitochondrial membrane potential and reduced mitochondrial size and branching[8]. Inhibition of complexes I and III simultaneously increased mitochondrial fission leading to more fragmented smaller mitochondria for degradation by mitophagy[9]. Recent developments in the field of high-throughput imaging and analysis have enabled the extraction of large number of cell images and a broad range of morphological features related to the shape, size, texture and spatial distribution of cells and their components, such as mitochondria[10]. Combining multiple morphological features provides a comprehensive and unbiased method for grouping cells with similar pathologies, thereby detecting cell clusters with similar modes of action, and predicting specific cellular pathologies[11]. This method has significantly contributed to identifying novel insights into disease etiology, mechanisms of action, new therapeutics, and toxicology predictions over the past decade[12–14] .

To determine whether morphology-based analysis can be used to distinguish the effects of different mitochondrial insults, we used known specific inhibitors - rotenone, antimycin, and oligomycin to inhibit complexes I, III, and ATP synthase using human induced pluripotent stem cell (iPS) - cortical neurons that are commonly studied in neurodegenerative disease research. We took a stepwise approach to analyse mitochondria at group-level and single-cell level. Group-level analysis involved analysing all cells treated with a mitochondrial function inhibitor. This analysis was performed using hierarchical clustering analysis that involves clustering cells according to their overall morphological similarities in response to mitochondrial inhibitors. This approach provided a broad understanding of how different treatments affected group of cells. Further, to capture cellular heterogeneity, we applied dimensionality reduction techniques such as Principal Components Analysis (PCA) and Uniform Manifold Approximation and Projection (UMAP) for detailed single-cell analysis. These techniques highlighted the subtle variations between single cells exposed to the same mitochondrial function inhibitor, identifying cells that exhibited strong responses to the inhibitors. By focusing on these highly responsive cells, we performed differential expression analysis of mitochondrial morphological features to identify specific morphological features that were significantly altered by each inhibitor treatment. We also applied machine-learning based prediction to forecast mitochondrial dysfunction outcomes more accurately.

This comprehensive approach of using high-throughput imaging for the acquisition of a large number of cell images, extraction of a diverse range of morphological features related to the shape, size, texture, and spatial distribution of mitochondria, combined with in-depth unsupervised and supervised machine-learning analysis at both the group and single-cell levels, encompasses "mitochondrial morphomics", which allows for an unbiased analysis of mitochondrial morphology leading to new insights into mitochondrial biology as described here.

Result section

Inhibition of mitochondrial complexes I, III and ATP synthase reduces mitochondrial respiration

To ensure that the mitochondrial complex inhibitors successfully inhibited mitochondrial respiration, we used the extracellular oxygen consumption assay. Human induced pluripotent stem cell (iPS) differentiated cortical neurons were treated with three inhibitors: rotenone, antimycin, and oligomycin, which target complexes I, III, and ATP synthase, respectively (Fig. 1A). Each inhibitor was tested at three concentrations (0.625 μM, 1.25 μM, and 2.5 μM). Measurements of extracellular oxygen consumption rate showed that all mitochondrial inhibitors significantly reduced mitochondrial respiration compared to healthy neurons ($p < 0.0001$; Fig. 1B).

Group-level cell hierarchical clustering analysis reveals distinct responses to mitochondrial complex inhibitions

To test whether our mitochondrial morphology assessment approach could distinguish the effects of different mitochondrial complex inhibitors on cells, we treated iPS-cortical neurons with rotenone, antimycin, and oligomycin to inhibit complexes I, III, and ATP synthase activity, respectively. Dimethyl sulfoxide (DMSO) was used as a vehicle for these drug treatments, and thus DMSO-treated cells served as controls. Figure 2A shows representative images of neurons treated with the highest concentration of each inhibitor, labelled with Tetramethylrhodamine, methyl ester (TMRM) to identify mitochondria, calcein to identify viable cells, and Hoechst to identify nuclei. TMRM accumulates in healthy mitochondria with an intact mitochondrial membrane potential, which is critical for ATP synthesis. For visual inspection of mitochondrial morphology at high resolution, we captured high-magnification images at 60x (Supplementary Fig. 3). In all inhibitor treatment conditions (Supplementary Fig. 3B-D), mitochondria appeared more fragmented and less elongated compared to the control. The differences between inhibitor effects were visually not striking, but Rotenone and Antimycin treatments (Supplementary Fig. 3C, D) showed a trend towards a more pronounced reduction in TMRM intensity compared to Oligomycin (Supplementary Fig. 3B). To objectively compare the inhibitor effects, we performed quantitative analysis. For quantitative high throughput imaging and analysis, the experiments were performed using a 20x objective. Using these cell images, we extracted morphological features related to mitochondrial size, shape, texture, and spatial distribution for each single cell[15]. In total, we extracted 50 morphological features from 55,577 single cells, resulting in 2,778,850 feature values for analysis. We then applied hierarchical clustering analysis to group cells based on their morphological features and visualise these groupings using a heatmap. Hierarchical clustering works by progressively grouping cells based on the similarity

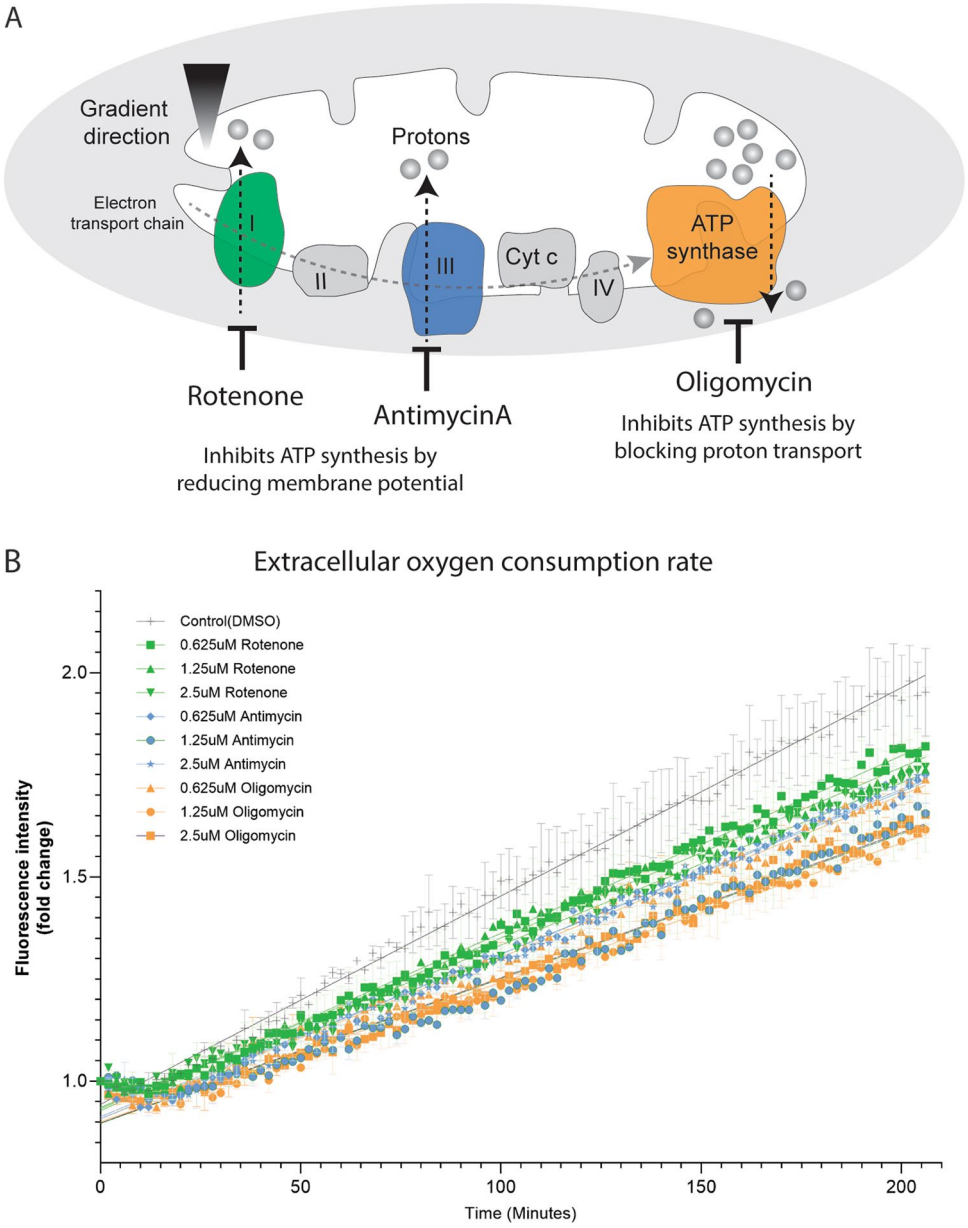

Fig. 1. Impact of mitochondrial complex inhibitors on cellular respiration and mitochondrial function. (**A**) Diagram of the mitochondrial oxidative phosphorylation related protein complexes and its connection to ATP synthesis. Mitochondrial membrane potential is maintained by the transfer of electrons through protein complexes I, III and IV in the inner mitochondrial membrane. As the electrons are transferred, protons are pumped across the inner membrane from the mitochondrial matrix into the intermembrane space, creating a proton gradient. The gradient created by this proton outflow subsequently brings protons back into the mitochondrial matrix via ATP synthase to generate ATP by phosphorylating ADP. (**B**) Mitochondrial respiration was measured by evaluating the extra cellular oxygen consumption. For this well-based time-series assay, 10,000 cells were seeded per well of a 96 well plate, and three experimental replicates were performed per condition. Cells with reduced mitochondrial respiration exhibit a relatively lower rate of oxygen consumption. Data presented as mean ± SD.

of their morphological features, creating a tree-like structure where cells that share similar characteristics are grouped together at different levels of the hierarchy.

Figure 2B shows a heatmap of hierarchical clustering analysis. In the heatmap, each row represents a group of cells (such as those treated with different inhibitors), and each column represents an aggregated mitochondrial morphological feature (for example mitochondrial area in a group of cells). Each square reflects the relative value of a specific feature for a given group of cells (for example antimycin treated cells) compared to all groups of cells. Cell groups with higher feature values are represented by more intense colours (red), while lower feature values are shown with less intense colours (blue). This color-coding allows for easy visualization of patterns in the

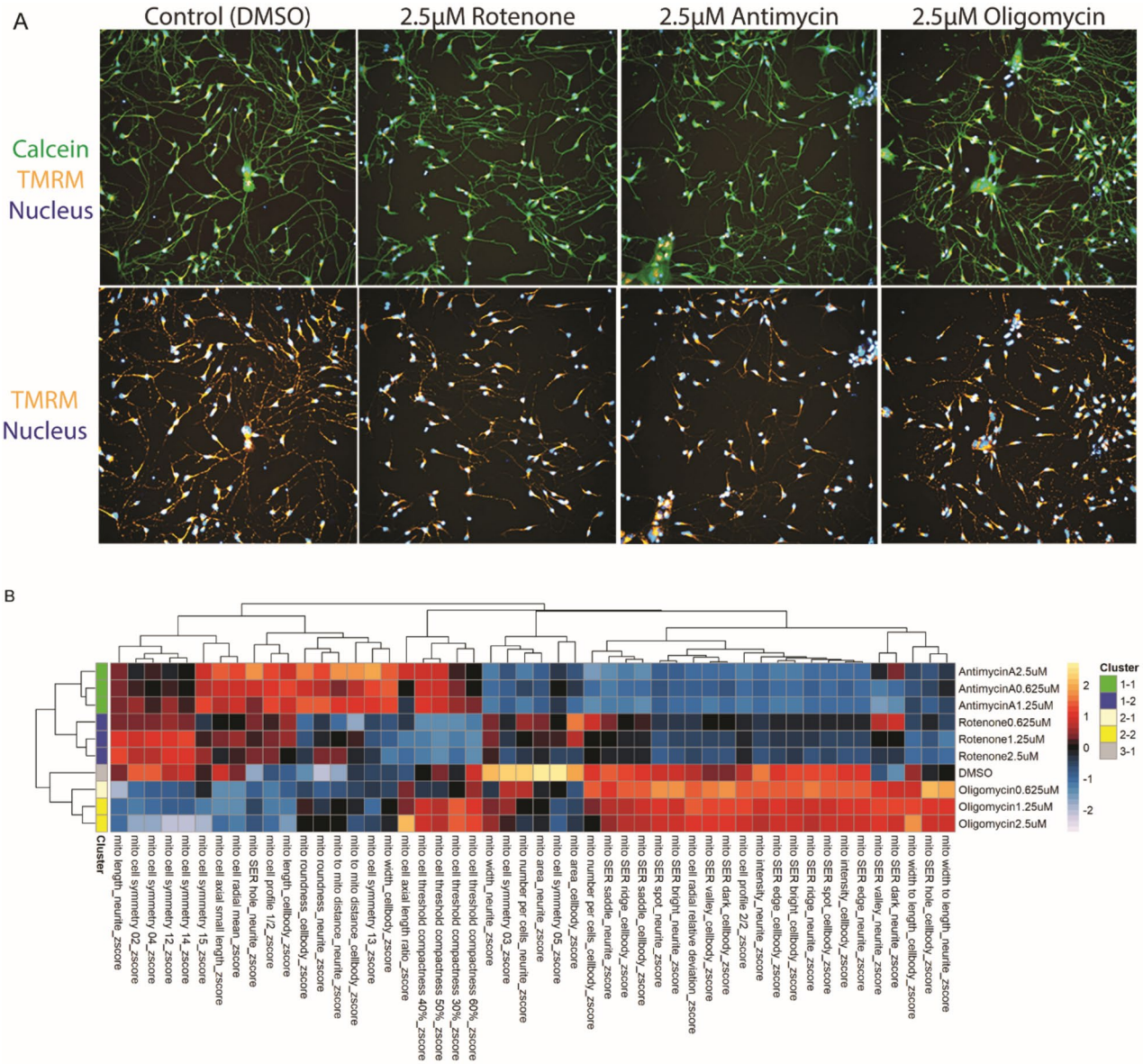

Fig. 2. Group-level cell hierarchical clustering analysis reveals distinct responses to mitochondrial complex inhibitions. (**A**) Representative fluorescent images of neuronal cells treated with Control (0.25% DMSO), 2.5 μM Rotenone, 2.5 μM Antimycin, and 2.5 μM Oligomycin. Cells were stained with Calcein (green), TMRM (orange), and DAPI (blue) to visualize the mitochondria, mitochondrial membrane potential, and nuclei, respectively. The upper panel shows Calcein staining, while the lower panel shows TMRM staining to highlight differences in mitochondrial membrane potential among the treated groups. (**B**) Heatmap showing hierarchical clustering of cells based on mitochondrial morphological and functional features after treatment with mitochondrial complex inhibitors. The clustering separates treatment groups based on the most-affected mitochondrial features. The coloured bar on the right represents different clusters (green, blue, yellow, grey), correlating with distinct cellular responses to mitochondrial complex inhibition. Sample numbers for each treatment group: DMSO ($n = 6072$), Antimycin 0.625μM ($n = 5927$), Antimycin 1.25μM ($n = 5247$), Antimycin 2.5μM ($n = 4748$), Rotenone 0.625μM ($n = 6908$), Rotenone 1.25μM ($n = 5174$), Rotenone 2.5μM ($n = 5802$), Oligomycin 0.625μM ($n = 6395$), Oligomycin 1.25μM ($n = 5860$), and Oligomycin 2.5μM ($n = 5444$).

data, showing how different groups of cells respond to mitochondrial inhibitors in terms of their mitochondrial morphology.

The hierarchical clustering dendrogram in Fig. 2B shows how cells treated with different mitochondrial complex inhibitors are grouped based on their morphological feature similarity. Clusters 1–1 and 1–2 (annotated in green and blue) represent cells treated with rotenone and antimycin, respectively. Both inhibitors target distinct components of the electron transport chain - complex I for rotenone and complex III for antimycin—but their effects converge on the disruption of electron flow, which is crucial for maintaining mitochondrial membrane potential. As a result, the cells treated with these inhibitors share similar changes in mitochondrial

morphological characteristics, indicating a common underlying response to the inhibition of electron transport, which leads to their grouping in neighbouring clusters. In contrast, clusters 2 – 1 and 2–2 (light yellow and yellow) represent cells treated with oligomycin, which targets ATP synthase. These cells grouped separately due to their distinct morphological response. Oligomycin directly inhibits proton flow into the mitochondrial matrix and it affects ATP production via a different mechanism than rotenone and antimycin. This functional difference is reflected in the mitochondrial morphology of these cells, leading them to cluster separately from those treated with electron transport chain inhibitors.

Additionally, within each cluster, cells treated with different doses of the same inhibitor tend to group closely together. For example, cells treated with varying concentrations of oligomycin (clusters 2 – 1 and 2–2) form sub-clusters within the larger group. This pattern suggests that while the dose of the inhibitor influences mitochondrial morphology, the overall response to the drug remains consistent across concentrations. The hierarchical clustering method effectively captures these subtle dose-dependent variations, demonstrating that the mitochondrial morphological changes induced by different doses of the same drug are related but can still be differentiated, reflecting the drug's concentration-dependent impact on mitochondrial function.

Identification and differential expression of single cells to mitochondrial complex Inhibition

Single cell-based data analysis is highly valuable for understanding the heterogeneity of cell populations, which can often be overlooked when analysing aggregated group or well-based values[16]. We analysed single-cell data to identify and visualize the most affected cells by specific mitochondrial complex inhibitions, such as antimycin, by observing distinct clustering patterns compared to controls and other treatments. This approach not only allows for statistical analysis but also enables the visual inspection of the cellular changes induced by each treatment. Additionally, the most affected cells can be used to enhance machine learning-based training and modelling strategies.

We further analysed the same dataset used for group-based hierarchical clustering which had 2,778,850 morphological feature values. Analysing such large single-cell datasets requires the adaptation of advanced data analysis approaches, such as dimension reduction techniques, which simplify and enhance the interpretation of complex data and aid in visualization[17]. PCA reduces the dimensionality of the data by transforming the original variables into a smaller set of uncorrelated components called principal components (PC). These principal components are linear combinations of the original variables, and they are arranged in such a way that the first few components capture the maximum variance present in the data. As shown in Fig. 3A, the top 10 PCs explained the majority of the variance in our data. Figure 3B presents the composite PCA scores (based on the top 10 PCs) for cells treated with different mitochondrial inhibitors (Antimycin, Rotenone, and Oligomycin) across three concentrations (0.625 µM, 1.25 µM, and 2.5 µM). The aggregated PCA scores show clear distinctions between control (DMSO) and inhibitor-treated cells, reflecting the unique effects of each inhibitor on mitochondrial morphology. These effects are dose-dependent, with higher concentrations (2.5 µM) leading to greater shifts in the composite PCA scores.

To further explore and visualise the complex relationships identified by PCA, we applied UMAP, a powerful dimensionality reduction technique particularly effective for visualizing high-dimensional data in two-dimensional space. This approach allowed us to plot the distribution of single cells based on the top 10 principal components. UMAP results are visualized in scatter plots, where similar data points are positioned close to each other. To gain an overall understanding of the response patterns for each inhibitor, we first examined the aggregated UMAP scores (Fig. 3C). These aggregated scores provide a summary of the collective cellular response to each treatment. To explore the underlying cellular heterogeneity that contributes to these aggregated patterns, we then plotted and analysed the single-cell data. The UMAP distribution of control single cells (DMSO, Fig. 3D) and single cells treated with antimycin (Fig. 3E), rotenone (Fig. 3F), and oligomycin (Fig. 3G) revealed distinct clusters corresponding to varying levels of cellular sensitivity to these treatments. Specifically, the analysis identified both the most affected and less affected cell populations within each treatment group. The most affected cell populations were clearly visualized in the density plots (Fig. 3H-K), which highlighted dense clustering (red) in specific regions of the UMAP space, indicating a strong and uniform response to each inhibitor. In contrast, the less affected populations were more dispersed, as depicted by less dense regions (yellow and green) in the density plots, suggesting a weaker or more heterogeneous response. Figure 3L-O shows representative images of cells belonging to the most affected cell populations after treatment with mitochondrial inhibitors. These images highlight the distinct morphological alterations observed in the highly impacted cells, including changes in mitochondrial structure, distribution and intensity. The visual representation confirms the significant cellular changes captured in the PCA and UMAP analyses, particularly for cells exposed to higher concentrations of antimycin, rotenone, and oligomycin.

We further focused our analysis on the single cells that were most affected by a specific inhibitor treatment rather than analysing all single cells to better understand the severity of the inhibitor treatments. Calculation of the median effect size, a measure that quantifies the magnitude of difference between groups, showed that the ATP synthase-inhibited cell group was relatively less affected compared to complex I and III inhibited cell groups (median effect size: 2.5µM rotenone: 0.14; 2.5µM antimycin: 0.08; 2.5µM oligomycin: 0.04). To determine the specific mitochondrial morphological features that were most affected by each inhibitor, we conducted a differential expression analysis. As shown in Fig. 3P-R, antimycin and rotenone resulted in greater disruptions in neurite-related features, such as mito_SER_spot_neurite and mito_intensity_neurite, with log *P*-values of 250 for antimycin and 225 for rotenone. In contrast, cell body -related features like mito_intensity_cellbody and mito_SER_edge_cellbody were less impacted, with log P-values below 150. Oligomycin showed a more moderate effect on both neurite and cell body features, with all log P-values remaining below 150.

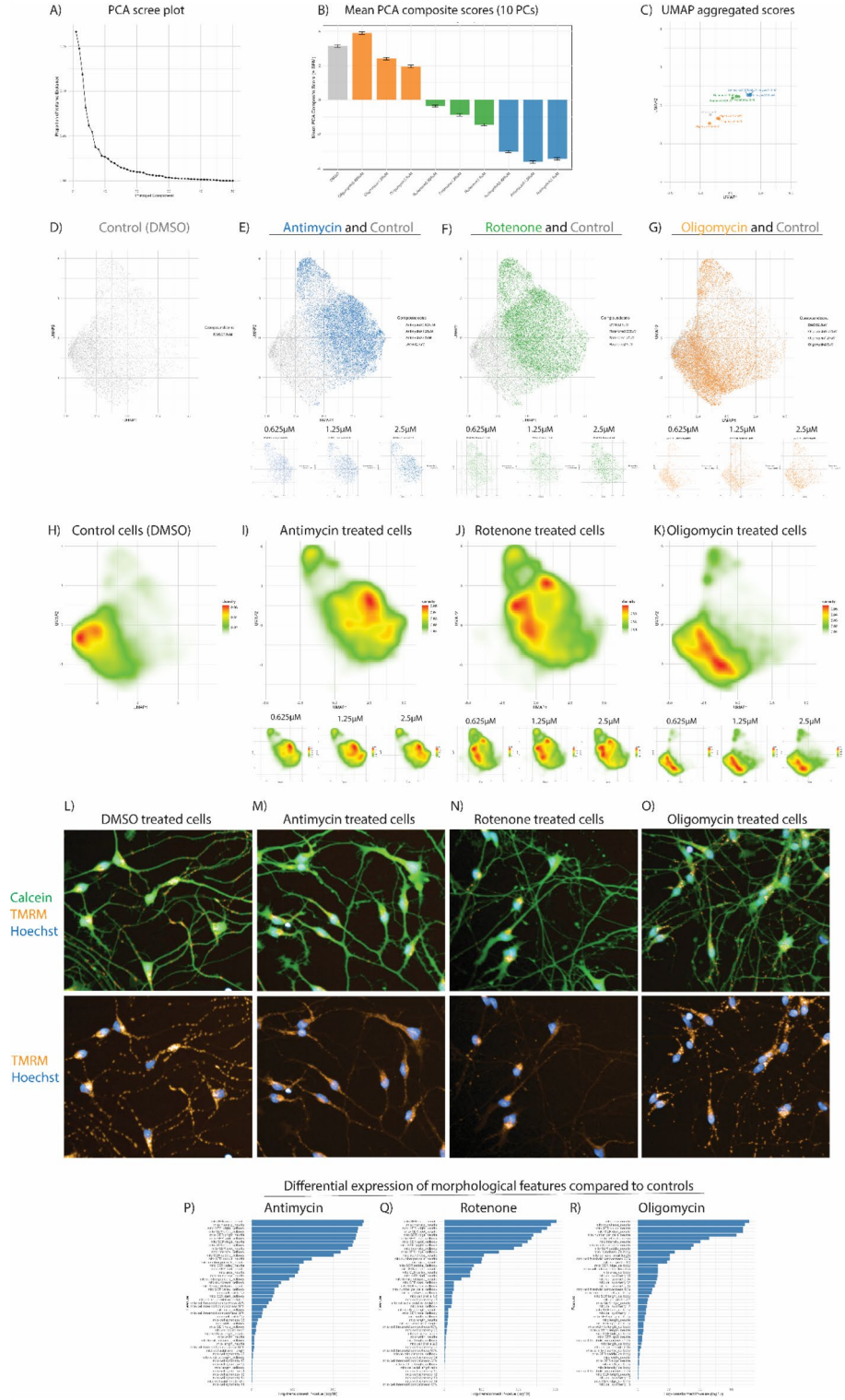

Enhanced prediction of mitochondrial Inhibition outcomes by targeting the most affected single cells

To determine if our single-cell analysis approach, which focuses on identifying the most affected cells by mitochondrial inhibitors, could enhance prediction accuracy, we compared machine learning-based predictions using data from all cells versus only the most affected cells for each inhibitor (2.5 µM rotenone, 2.5 µM antimycin, and 2.5 µM oligomycin). Overall, by targeting only the most affected single cells, prediction accuracy improved for each inhibitor: from 62.75 to 81.97% for antimycin, from 71.86 to 75.12% for rotenone, and from 86.72 to 94.42% for oligomycin (Fig. 4A, B). Furthermore, this approach reduced the misclassification of antimycin as rotenone decreased from 31.2 to 16.36%, which directly contributed to the marked improvement in antimycin prediction accuracy. These results highlight the importance of focusing on cellular heterogeneity and utilising

◂**Fig. 3**. Identification and differential expression of a sub-population of most affected single cells in response to mitochondrial complex inhibition. (**A**) PCA scree plot illustrating the variance captured by each principal component in the dataset, indicating dimensionality reduction. (**B**) Composite PCA scores (based on the top 10 PCs) for cells treated with different mitochondrial inhibitors (Antimycin, Rotenone, and Oligomycin) across three concentrations (0.625 μM, 1.25 μM, and 2.5 μM). (**C**) UMAP visualization of aggregated scores, displaying separation of cell populations based on treatment conditions: DMSO, Antimycin, Rotenone, and Oligomycin at different concentrations (0.625 μM, 1.25 μM, and 2.5 μM). (**D**–**G**) UMAP plots showing the comparison between DMSO-treated control cells (**D**) and cells treated with Antimycin (**E**), Rotenone (**F**), and Oligomycin (**G**) at varying concentrations. (**H**–**K**) Heatmaps depicting the density of high-responsive cells across different treatments: control cells (DMSO) (**H**), Antimycin-treated cells (**I**), Rotenone-treated cells (**J**), and Oligomycin-treated cells (**K**). The heatmaps highlight regions of high cellular response (red region). (**L**–**O**) Fluorescence images of DMSO high-responsive cells (**L**), Antimycin high-responsive cells (**M**), Rotenone high-responsive cells (**N**), and Oligomycin high-responsive cells (**O**). Cells are stained with Calcein (green), TMRM (orange), and Hoechst (blue) to highlight mitochondria, mitochondrial membrane potential, and nuclei, respectively. (**P**–**R**) Differential expression of morphological features compared to controls for Antimycin (**P**), Rotenone (**Q**), and Oligomycin (**R**) treatments. Bar plots represent the top morphological features contributing to the cellular response under each treatment condition.

A **Prediction based on all single cells**

True label \ Predicted label	Rotenone	Antimycin	Oligomycin
Rotenone	71.86	20.72	7.44
Antimycin	31.2	62.75	6
Oligomycin	8.77	4.4	86.71

B **Prediction based on sub-population of cells**

True label \ Predicted label	Rotenone	Antimycin	Oligomycin
Rotenone	75.11	17.79	5.11
Antimycin	16.36	81.96	0.75
Oligomycin	5.71	0.38	94.41

Fig. 4. Improved prediction of mitochondrial inhibition outcomes using a sub-population of the most affected single cells. (**A**) Confusion matrix showing the prediction accuracy of mitochondrial complex inhibition outcomes (Rotenone, Antimycin, and Oligomycin) based on all single cells. The matrix indicates classification performance with true labels on the y-axis and predicted labels on the x-axis. (**B**) Confusion matrix showing the improved prediction accuracy of mitochondrial inhibition outcomes using a sub-population of the most affected single cells. The classification performance is notably enhanced compared to predictions based on all single cells.

the most responsive cells to achieve more accurate predictions of mitochondrial dysfunction outcomes induced by complex I, III, and ATP synthase inhibition.

Discussion

In this study, we treated iPS-neurons with three modulators of mitochondrial oxidative phosphorylation: rotenone (complex I inhibitor), antimycin (complex III inhibitor), and oligomycin (ATP synthase inhibitor). The functional assay measuring mitochondrial respiration showed that all three inhibitors consistently reduced respiration, as expected given their roles in ATP synthesis, but it did not differentiate the specific effects of each inhibitor at the concentrations tested here. Our high throughput imaging and data analysis approach distinguished the effects of each mitochondrial inhibitor. We took a stepwise approach to analyse mitochondria at both the group and single-cell levels. Hierarchical clustering analysis of cells treated with different complex inhibitors, i.e., complex I, III and ATP synthase, clustered all cell groups differently from each other and from control cells, showing the capability of our analysis approach in detecting cells with different mitochondrial dysfunctions. Extended analysis of single cell-based data helped us to appreciate cellular heterogeneity and identify the proportion of cells predominantly affected by each mitochondrial complex inhibitor based on a collective set of morphological features. Identification of the most affected cells had two major applications: (1) identification of the morphological features specifically affected by each mitochondrial inhibitor and (2) enhanced prediction accuracy of single cells with mitochondrial dysfunction. Differential expression analysis showed that consistent with their mode of action, complex I and III inhibitors, which disrupt the electron transport chain, exhibited a similar pattern of morphological feature alterations, though with varying degrees of severity. In contrast, ATP synthase inhibition resulted in more subtle and distinct effects, characterized by relatively smaller changes in membrane potential, thus highlighting the distinct effects of mitochondrial inhibitors based on their mode of action. To further validate the utility of the morphological features identified in our analysis, we applied machine-learning techniques to predict mitochondrial inhibition outcomes. Initially, predictions based on all cells yielded accuracies of 62.75% for antimycin, 71.86% for rotenone, and 86.72% for oligomycin. However, by focusing specifically on the most affected cells, as identified through the single-cell analysis, prediction accuracy improved to 81.97% for antimycin, 75.12% for rotenone, and 94.42% for oligomycin. Second, and perhaps more importantly, this approach reduced the misclassification of closely related inhibitors, such as antimycin and rotenone, which both target the electron transport chain. The misclassification of antimycin as rotenone decreased from 31.2 to 16.36%, which directly contributed to the marked improvement in antimycin prediction accuracy. This finding underscores the utility of our approach in resolving phenotypic overlaps that arise from shared pathways, such as the electron transport chain. This marked improvement in the prediction accuracy highlights the importance of targeting the sub-population consisting of most affected cells, underscoring the value of our approach in enhancing the precision of modelling mitochondrial dysfunction. This method has the potential to significantly improve the evaluation of mitochondrial modulators and therapeutic interventions.

The effects of the mitochondrial complex inhibitors here concur with previous studies. HepG2 cells were treated with 12 doses of rotenone (complex I inhibitor), antimycin (complex III inhibitor), and oligomycin (ATP synthase inhibitor) ranging from 0.0001 to 50μM[18]. Assessment of ATP content, membrane potential and mitochondrial morphology over 24 h using high throughput imaging microscopy showed that all inhibitor treatments, particularly at doses above 0.01μM, reduced cellular ATP content. However, the treatments had distinct effects on mitochondrial membrane potential and morphology. Complex I and III inhibition significantly reduced membrane potential, while ATP synthase inhibition did not affect or mildly increased membrane potential. Evaluation of mitochondrial size to understand mitochondrial fission showed that ATP synthase inhibition but not complex I and III inhibitions increased mitochondrial fission[18]. Similar to our findings, while all mitochondrial complex inhibitors reduced ATP, they had distinct effects on mitochondrial membrane potential and morphology, highlighting the possibility of using mitochondrial membrane potential and morphology measures to classify inhibitor effects based on their modes of action. Similarly, in iPS-derived neurons, inhibition of complex I and not ATP synthase reduced membrane potential[19]. In addition to the primary effects of complex inhibition on mitochondrial ATP synthesis, secondary effects of mitochondrial dysfunction, such as reactive oxygen species production, can also contribute to the observed changes in mitochondrial morphology[20].

Mitochondria are dynamic organelles that change size and shape to perform various cellular functions[4,7]. The correlation between mitochondrial morphology - shape, structure, network, and spatial distribution—and function is well-established and referred to as 'morphofunction'[9,21]. This relationship is bidirectional and linked to multiple mitochondrial roles[22,23]. Mitochondrial morphology is modulated by processes such as fusion, fission, motility, and interactions with other organelles[4,5]. Under stress, such as exposure to mitochondrial toxins, mitochondrial fusion helps balance ATP production by combining damaged mitochondria with healthy ones, while fission isolates and removes dysfunctional parts for degradation through mitophagy. These processes ensure energy production and quality control, maintaining cellular homeostasis. An imbalance in the fusion: fission ratio is commonly observed in neurodegenerative disease patient-derived cells[24]. Along with these processes, mitochondrial dynamics and morphology are determined by mitochondrial cristae structure governed by its protein and lipid composition. The folding and topology of the inner membrane, where electron transport chain complexes and ATP synthase dimers reside, are crucial for bioenergetics[25] where cristae remodelling enhances energy production[26,27]. Downregulation of phosphatidylethanolamine, a phospholipid critical to maintaining mitochondrial membrane structure in CHO-K1 cells, induced formation of more rounded cristae, reduced complexes I and IV activity, impaired super complex formation, reduced ATP synthesis, higher mean mitochondrial circularity, and increased mitochondrial fragmentation[28]. Mitochondrial matrix configuration is also dynamic, governed by membrane potential, with complex I inhibition simultaneously decreasing membrane potential and increasing matrix condensation[29].

Given the complex and highly dynamic nature of mitochondria, we utilized a high throughput imaging and analysis approach that allows extraction of a large number of morphological features - including parameters such as shape, size, texture, and spatial distribution. These features enabled us to perform a comprehensive mitochondrial morphological analysis and capturing subtle changes in mitochondrial structures. These extensive features provided a rich dataset of 2,778,850 feature values from 55,577 single cells for an unbiased, high-resolution analysis of mitochondrial alterations induced by different complex inhibitors. First, by applying hierarchical clustering analysis, we were able to distinguish cells at a group-level based on their morphological responses to the mitochondrial inhibitors - rotenone, antimycin, and oligomycin. This method allowed us to cluster cells treated with each inhibitor distinctly from one another and from control cells, showcasing the application of multiparametric analysis in detecting diverse patterns of mitochondrial dysfunction that are often obscured in traditional bulk measurements, such as the mitochondrial respiration assay shown in result Sect. 1. Multi-parametric analysis approaches have been successfully applied in the recent past to better understand mitochondrial biology. Using live cell imaging, Westrate et al., were able to predict mitochondrial fusion and fission events by evaluating their morphological features. Mitochondrial perimeter correlated positively with fission and mitochondrial solidarity with fusion[30]. Charrasse et al.. analysed the effects of a range of pesticides on lung epithelial cells using 104 parameters, including 24 mitochondrial features and 26 features of mitochondrial clusters (shape, intensity and spatial descriptors)[31]. By analysing these features in combination using unsupervised PCA and supervised linear discriminant analysis machine-learning approaches, the authors identified a specific mitochondria morphological signature for each individual pesticide. Morphological assessment of other cellular components such as the nucleus did not identify any significant alterations at moderate doses indicating the specificity of mitochondrial inhibition effect on mitochondrial morphology[32]. Similarly, our analysis did not affect nucleus morphology.

Group-level cell analysis helps identify overall trends and morphological patterns across cell populations, as seen here, but fails to provide information on subtle changes of individual features, cumulative effects of these subtle changes or heterogeneous responses. While it helps in classifying large groups of cells based on similar responses, it misses the finer details of cell-to-cell variability. This is relevant to neurodegenerative disease pathology assessment. A genetic mouse model of Parkinson's disease with mitochondrial dysfunction selectively in dopaminergic neurons demonstrated that mitochondrial morphology defects preceded both neuronal impairment and motor deficits. These early mitochondrial abnormalities also responded to treatment, highlighting their potential as early indicators of disease progression and therapeutic efficacy[33]. To assess mitochondrial morphology, mitochondria were classified into four distinct types based on their morphology: type I mitochondria - healthy mitochondria, type II mitochondria - moderately affected mitochondria, type III mitochondria - severely affected mitochondria and type IV mitochondria - dysfunctional mitochondria exhibited disrupted outer membrane, deficiency in cristae, absence of the internal membrane structures[33]. In this study, mitochondrial morphology was assessed across different disease stages - early, middle, and late, in both mutant and wild-type mice, with or without PT320 treatment a sustained release formulation of the GLP-1R agonist Exenatide, a therapeutic agent aimed at mitigating mitochondrial dysfunction. In wild-type mouse, at all disease stages, the population of type I mitochondria was consistently present at ~ 80% and had ~ 20% of all other mitochondrial types i.e., types II, III and IV. The % of type I mitochondria was significantly lower in the mutant mouse in the early disease stage at ~ 30% and this further reduced to 20% and 15% in the middle and late disease stages respectively. The rest of the mitochondria belonged to types II, III and IV with type IV being about 50% of all mitochondria in the late stages. The presence of PT320 demonstrates a protective effect on mitochondrial morphology in the early and middle disease stages, where the % of type I mitochondria was comparable to wild-type mice[33]. Such understanding of mitochondrial dysfunction and drug treatment effects arising from measuring single mitochondrion which will be reflective in single-cell analysis can be missed or discounted with group-based analysis.

Along with group-level cell analysis, we analysed single-cell data using dimensionality reduction techniques - PCA and UMAP to understand the cellular heterogeneity of mitochondrial dysfunction. Dimensionality reduction simplified the complex, high-dimensional dataset, while still retaining the most important variance, helping to reveal the subtle differences between individual cells. Through this method, we were able to efficiently visualize clusters of single cells based on their unique morphological profiles, revealing subpopulations of cells that were more severely affected by the mitochondrial inhibitors. In contrast to group-level analysis, which averages responses across entire cell populations, single-cell analysis allowed us to capture the variability within individual cells and identify those cells most responsive to the inhibitors. This was especially important for understanding how mitochondrial dysfunction presents heterogeneously, often affecting a smaller sub-population of cells more dramatically than others within the same population. By focusing on these most affected cells, we could uncover distinct morphological features that were uniquely altered by each inhibitor, offering deeper insights into their mechanisms of action.

To refine these findings further, we employed differential expression analysis at the single-cell level, which allowed us to identify the specific morphological features that were significantly altered by each inhibitor. For both rotenone and antimycin, the single-cell analysis showed that neurites were more severely impacted than the cell body, with features such as mito_SER_spot_neurite and mito_intensity_neurite being significantly affected. This indicates that neurites, which have higher energy demands, are particularly vulnerable to disruptions in mitochondrial function. In contrast, cell bodies showed fewer alterations, suggesting that mitochondrial dysfunction in neurites may be an early marker of mitochondrial stress before the cell body is compromised. This neurite vs. cell body distinction is a unique advantage of single-cell analysis, as group-level approaches would have averaged these effects across the entire cell population, missing these important region-specific vulnerabilities. In contrast, oligomycin (ATP synthase inhibitor) exhibited a distinct profile, where the neurites were again predominantly affected, particularly in terms of fission and membrane potential, indicating that

ATP production in the neurites is crucial for maintaining their health. The ability to discern compartmentalized mitochondrial dysfunction - such as in the neurites versus the cell body—was made possible only through single-cell resolution. This capability demonstrates the advantage of single-cell analysis in detecting subtle, compartment-specific mitochondrial responses, which is crucial in diseases where neuronal dysfunction is driven by localized mitochondrial impairments. However, it is important to note the limitations of our study. While we focused on mitochondrial morphology in this work, interactions between mitochondria and other sub-cellular components, such as lysosomes, were not assessed. These organelle-organelle interactions are known to influence mitochondrial function and could provide additional insights into the mechanisms of dysfunction. Future studies involving the assessment of multiple organelles together are warranted.

Finally, the predictive power of our approach was enhanced by narrowing the analysis to the most affected cells. By focusing the machine learning models on these cells, rather than using data from all cells, we were able to increase the prediction accuracy of mitochondrial dysfunction outcomes. This improvement in accuracy highlights the importance of focusing on the most responsive subpopulations rather than averaging over all cells, as bulk analyses would have obscured these critical cellular responses. The ability to target the most affected cells provides a more accurate understanding of mitochondrial health and dysfunction, making it a valuable tool for both drug evaluation and the future development of therapeutic interventions in diseases associated with mitochondrial dysfunction. Our approach of identifying a sub-population of most affected cells is novel and not shown in previous studies involving iPS-neurons[34].

In conclusion, in this study, single-cell analysis of mitochondria provided a high-resolution view of cellular heterogeneity in response to mitochondrial inhibitors, revealing subpopulations of cells most affected by each treatment. By focusing on these most responsive cells, helped us identify distinct morphological features that were specifically altered by an inhibitor, leading to more accurate predictions of mitochondrial dysfunction outcomes. This approach highlights the value of targeting specific subpopulations for a precise understanding of mitochondrial health and drug efficacy, offering a potential tool for evaluating therapeutic interventions in neurodegenerative diseases associated with mitochondrial dysfunction.

Methods

Ethics This study involving human cells was reviewed and approved by the Human Research Ethics Committee at University of New South Wales, Australia (reference number: iRECS4567). Research involving the generation of iPS stem cells was approved by the Gene technology office at University of New South Wales, Australia (reference number: NLRD-GTRC-2023-0652). All experiments were carried out in accordance with relevant guidelines and regulations.

Reprogramming of human peripheral blood mononuclear cells (PBMCs) to iPS cells

iPS cells were generated by reprogramming commercially purchased PBMCs (07930, Stem cell technologies) as described by us previously[1]. Briefly, PBMCs were genetically reprogrammed using commercially available CytoTune-iPS Sendai reprogramming kit vectors KLF 4, c-MYC, SOX 2 and OCT 3/4. iPS cells were stored in a cryotank until required for the neuron differentiation experiments.

Differentiation of iPS to mature cortical neurons and charecterisation

iPS cells were differentiated into cortical neurons using the dual SMAD induction and FGF2 expansion protocol for 30 days using previously published protocols[1,35]. To characterise the mature neurons generated, we tested the presence of mature cortical neuron markers TBR1 and CTIP2 [36,37] by immunostaining using our previously published protocol[1]. Briefly, the cells were fixed, permeabilised and immunostained using the BD Cytofix/Cytoperm™ Fixation/Permeabilization Kit (Cat#554714, BD Biosciences). Primary (TBR1, ab183032, Abcam and CTIP2 ab18465, Abcam) and secondary antibody incubations were performed for 1 h and 30 min respectively. 90% of cells expressed beta III tubulin, a marker for neurons, 32% of the cells expressed TBR1, a mature cortical layer VI marker and 28% of the cells expressed CTIP2, a mature cortical layer V marker (Supplementary Fig. 1) confirming their mature cortical neuron identity.

Mitochondrial inhibitor treatment

Rotenone (Cat# R8875, Sigma), antimycin A (Cat# A8674, Sigma) and oligomycin A (Cat# 75351, Sigma) were used to inhibit electron transport chain complexes I and III and ATP synthase, respectively. Three different doses were used for each inhibitor: 0.625μM, 1.25μM and 2.5μM. All the inhibitors were prepared in dimethyl sulfoxide (DMSO) (102952, Sigma). The untreated cells were cultured in 0.25% DMSO, the highest DMSO concentration used to prepare the inhibitors, to account for any cellular effects arising by DMSO exposure. All inhibitor treatments were performed for 16 h.

Live cell mitochondria morphology assay

After 16 h of drug media containing drugs was removed and replaced with a PBS+/+ staining solution for various cells components (Calcein AM, C3100MP, 1:2000; Hoechst, 33342, 1:10,000 and TMRM, T-668, 25nM, all Thermofisher scientific products) and incubated for 30 min at 37°C. Staining solution was then replaced with PBS+/+ and imaged with Operetta at 20x magnification. Calcein AM is used to label and identify viable cells. Calcein AM is non-fluorescent and can cross the cell membrane due to its lipophilic nature. The presence of cytosolic unspecific esterase cleaves down the acetomethoxy group (AM) to form Calcein that become fluorescent. By its nature, this hydrophilic alcohol is not permeable to membranes and, consequently, the molecule is retained in the cell cytosol. When excited, calcein exhibits green fluorescence. Hoechst is used to label and identify nuclei. Hoechst is composed of multiple molecules that can diffuse through membrane due to its small size and positive charge, Hoechst, a non-intercalating molecule, binds to the minor groove of double-

stranded DNA, with a preference for A-T rich regions. Upon DNA binding, the suppression of rotational and reduction of hydration of the molecule diminish energy dissipation, increasing pre-existing blue fluorescence by 30. When excited, Hoechst exhibits blue fluorescence[38]. TMRM accumulates in mitochondria with high mitochondrial membrane potential and hence commonly used as an indicator for healthy mitochondria. It is a non-polar, fluorescent molecule that can easily diffuse inside the cell. It is positively charged and naturally attracted to the strong negatively charged mitochondrial matrix. As the dye accumulates inside mitochondria, a more intense fluorescence signal comes from healthy mitochondria compared to the background and the unhealthy mitochondria.

High-magnification images were acquired using the Revvity PhenixPlus confocal mode at 60x magnification. Z-stacks were captured with 0.5-micron steps. These images are presented in Supplementary Fig. 3.

Morphological feature extraction

The morphological features defined were extracted from cell images using the Harmony High-Content Imaging and Analysis Software (version 4.9, Revvity). The cell nucleus and the cells were identified based on Hoechst and calcein staining and using the "Find Nuclei" and "Find Cytoplasm" functions. Morphological features were extracted using the "Calculate Intensity Properties", "Calculate Morphology Properties" and "Calculate Texture Properties" functions. The morphology and texture features were extracted as described before[15]. Mitochondrial size and texture related features were extracted for different cell regions i.e., the cell body and neurites.

Developed in collaboration with specialists from Revvity, Inc (manufactures of the imaging and analysis platform used here), we leveraged our combined expertise in cellular morphomics and mitochondrial biology[1,15]to provide a comprehensive description of the morphological features extracted and their potential relevance to mitochondrial morphology and function.

Texture features

The texture features are based on the patterns and variations in pixel intensities across a cell image. Here, we use a set of eight texture filtered images quantifying the presence of different characteristic intensity patterns. The size of the pattern ("scale") corresponds to the size of the intensity features of interest (mitochondria or parts of it). These features are particularly helpful to access and indicate the complex mitochondrial structure. Some of those features are directly correlated to visible biological features (e.g., elongated mitochondria or vacuolated regions), while others are useful in combination in statistical analysis, helping to uncover less visible but biologically relevant patterns. Table 1 below provides a detailed description of the texture features in relevance to mitochondria and also the cell spatial organisation and distribution of mitochondria.

Extracellular oxygen consumption (OCR) assay

The OCR assay is a well-accepted measure of mitochondrial respiration. It measures cell oxygen use with a real-time kinetic analysis using a fluorescence probe. The assay kit (ab197243) comprises of an oxygen quenching fluorescent dye that is added to cell culture media. In cells with healthy mitochondria, high respiration rates lead to significant oxygen consumption, reducing local oxygen concentration. This results in a higher fluorescence intensity from the oxygen-sensitive probe. Vice versa for dysfunctional mitochondria. The experiments were performed following the manufacturer's instructions and according to published methods[39].The probe fluorescence was measured using fluorescence plate kinetic reader for 2 h at 37°C. The rate of change in fluorescence intensity was calculated, providing a measure of the oxygen consumption rate, indicating the mitochondrial respiration.

Hierarchical clustering for group-level cell analysis

This analysis was performed using RStudio R packages Spectre for data processing and clustering, and pheatmap for visualizing the results. *Data Pre-processing and Normalization*: The raw data were imported from a CSV file containing cellular features from multiple experimental conditions. The dataset included columns representing various morphological measurements across different treatment groups. Batch correction was applied using the ComBat function from the Surrogate Variable Analysis (sva) package, which corrects for non-biological variation across different experimental batches while preserving the biological differences between groups. After batch correction, the mean of each morphological feature was calculated within each treatment group. These features were then z-score normalized to ensure comparability across different scales. Missing values were replaced with 0. *Hierarchical Clustering*: Hierarchical clustering was performed on the z-score normalized data using Euclidean distance and Ward's method for linkage. The clustering was conducted in two stages: first, we performed hierarchical clustering to identify three main clusters. These clusters were further subdivided by applying hierarchical clustering within each main cluster to generate two sub-clusters, creating a total of six final clusters. The main and sub-cluster assignments were then combined to form unique cluster labels (e.g., 1–1, 1–2, etc.). The distance matrix for clustering was computed from the scaled feature data, and clustering was performed using the hclust function in R. To assign data points to clusters, the cutree function was used, specifying the desired number of main and sub-clusters. The results were stored in the dataset as new columns representing both main and sub-cluster assignments. *Heatmap Generation*: Heatmaps were generated to visualize the clustered data. The columns corresponding to the z-score normalized features were used for this purpose. Annotations based on the cluster assignments were added to each heatmap to facilitate the interpretation of the results. Custom colors were applied to the clusters to visually distinguish between them. Specifically, the following color scheme was used: 1–1 = green, 1–2 = blue, 2–1 = light yellow, 2–2 = yellow, 3–1 = grey. Heatmaps were generated using the pheatmap function, displaying the morphological features and cluster annotations. The R script file is available as Supplementary File. 4.

	Feature	Feature description and mitochondrial relevance
Texture features	Spot feature	Detects pixels where the intensity of the surrounding pixels drops in all directions on the given scale. This is represented by a decrease in intensity ('-' arrows), which may indicate mitochondrial fragmentation during fission. Supplementary Fig. 2A.
	Hole feature	Detects small dark regions where dark pixels are surrounded by bright pixels, representing a hole. This feature corresponds to a reduction in intensity ('-' arrows), indicating regions of lower intensity that could suggest mitochondrial vacuolation or cristae remodelling. Supplementary Fig. 2B.
	Ridge feature	Detects long, linear structures with clear boundaries based on pixel intensities. These are typically associated with an increase in intensity ('+' arrows), representing elongated, highly interconnected mitochondria. Supplementary Fig. 2C.
	Valley feature	Identifies elongated regions with pixels that have significantly lower intensity values compared to their surroundings. This decrease in intensity ('-' arrows) can be associated with mitochondrial dysfunction or structural damage. Supplementary Fig. 2D.
	Saddle feature	Detects regions with a combination of high and low intensities, creating a saddle-like intensity profile. This feature shows both increases ('+') and decreases ('-') in intensity, indicating complex mitochondrial structures, often seen during the fusion-fission transition. Supplementary Fig. 2E.
	Edge feature	Quantifies the total amount of edges inside the region of interest (e.g., cell bodies or neurites). Higher edge values indicate a more structured intensity pattern, while the presence of other texture features (such as ridges or valleys) will also increase the edge value. Supplementary Fig. 2H.
	Bright and dark features	Quantifies the presence of bright or dark plateaus larger than the given scale. These plateaus are typically characterized by constant intensity ('const'), with bright regions indicating larger smooth areas of high intensity and dark regions representing larger smooth areas of low intensity. Supplementary Fig. 2F, G.
STAR features	Threshold compactness	The "Threshold compactness" based cell assessment indicates if there are bright compact regions in the cell indicative of mitochondrial clustering/organisation. It does this by, first identifying the top 30–60% of bright pixels based on their intensity and then the compactness of the bright pixels in the cell is measured. This assessment indicates if the bright pixels are coming from a single compact area or fragmented into multiple smaller irregular regions. Mitochondrial relevance: Under certain physiological and pathological conditions, such as impaired axonal transport, mitochondria cannot be effectively transported to distal regions of the cell resulting in mitochondrial accumulation or clustering around the cell body where they are generated. Supplementary Fig. 2I.
	Symmetry	The "Symmetry" assessment indicates the symmetry of the mitochondrial intensity distribution within cells. It examines if the fluorescence intensity distribution in the cell is symmetrical. There are eight properties reflecting the symmetry of the intensity distribution inside each cell based on the intensity of radial decay and circular repetition patterns. Properties are named "Symmetry XY". X describes the intensity decay in radial directions – 0 and 1. 0 indicates how mitochondrial fluorescence intensity is distributed uniformly throughout the cell. 1 indicates how mitochondrial fluorescence intensity is distributed from the cell center to the periphery. Y reflects the number of circular repetitions. It indicates that the intensity pattern of mitochondria repeats Y number of times around the cell circumference. For example, Symmetry 02: Reflects a basic, bipolar symmetry where the mitochondrial intensity distribution pattern has two symmetrical regions. Symmetry 03, 04 and 05 indicate more complex tripolar, quadripolar and pentapolar intensity distribution patterns. Like Symmetry, the Radial (Supplementary Fig. 2D) and Profile (Supplementary Fig. 2E) assessments measure mitochondrial spatial distribution based on their intensity distribution. Supplementary Fig. 2J.
	Radial	The Radial measures are used to analyse the distribution of fluorescence intensity from the center of the cell outward. "Radial Mean" measures the average distance of mitochondria from the cell center, weighted by their fluorescence intensity. It indicates how mitochondria are distributed relative to the cell center. "Radial Relative Deviation" measures the variation in the radial distribution of mitochondrial intensity. It indicates the homogeneity or heterogeneity of mitochondrial distribution around the cell center. Supplementary Fig. 2K.
	Profile	Profile parameter analyses intensity distribution in the specific regions of the cell. The two specific profile regions we use are Profile 2/2 measures the intensity of mitochondria closer to the cell center or nucleus. Profile 1/2 measures the intensity of mitochondria closer to the cell periphery. Comparing the intensity profiles of both regions it can indicate if the mitochondrial distribution is more central or peripheral. Changes in these parameters can indicate mitochondrial distribution alterations. Supplementary Fig. 2L.

Table 1. Description of texture features and cell spatial organisation and distribution features.

Single cell-based analysis This analysis was performed using RStudio utilising these R packages were utilized: data.table for data handling, Spectre for data processing and clustering, ggplot2 and ggpubr for data visualization, umap for dimensionality reduction, and openxlsx for exporting results. Additional packages, such as cluster, MASS, and cowplot, were used to enhance clustering and visualization capabilities. *Data Pre-processing, transformation and normalization*: Raw data, containing cellular features from multiple experimental conditions, were imported from a CSV file. Batch correction was applied using the ComBat function from the Surrogate Variable Analysis (sva) package to correct for potential batch effects across different experimental plates. After batch correction, an Arcsinh transformation was applied to the feature columns to compress large values while preserving the structure of the data. Following the transformation, z-score normalization was applied to each feature, standardizing the values across different scales for comparability. Features with zero variance were removed to ensure that only informative variables were used in subsequent analyses. Dimensionality reduction - *Principal Component Analysis (PCA)*: PCA was performed on the transformed and normalized data to reduce dimensionality and identify key features contributing to variance. Scree plots were generated to illustrate the variance explained by each principal component. *UMAP Visualization*: UMAP was used to visualize the high-dimensional PCA scores. UMAP was applied to the first 10 principal components to create 2D representations of the data, facilitating the identification of patterns across different experimental groups. Aggregated UMAP plots were generated by calculating the mean UMAP scores for each group. Additionally, density-based UMAP plots were created to visualize the distribution of data points across different experimental conditions. *Identifying sub-population of cells that are most affected by an inhibitor treatment and differential expression analysis*: To identifying sub-population of cells that are most affected by an inhibitor treatment, cells around the median for each group were selected based on the median absolute deviation (MAD). Groups included in the analysis were "DMSO2.5uM", "AntimycinA2.5uM", "Oligomycin2.5uM", and "Rotenone2.5uM". A non-parametric Wilcoxon test was performed to compare each experimental group with the control group ("DMSO2.5uM") across selected features. P-values were adjusted using the Benjamini-Hochberg method, and effect sizes were calculated to quantify the differences between groups. Heatmaps were generated to visualize differential expression results and effect sizes across the experimental groups. Log-transformed P-values and effect sizes were visualized using bar plots. For significant results, log-transformed P-value plots were generated with a white background for clarity. Custom color palettes were applied to distinguish between experimental groups in both UMAP and heatmap visualizations. The R script file is available as Supplementary File. 5.

References for all R-packages used for group and single cell level analysis data.table, ggplot2 [40], ggrepel[41], rstudioapi[42], Spectre[43], viridis[44], ggpubr[45], UMAP[46], cluster[47], MASS[48] and cowplot[49].

Machine-learning based prediction and 10-fold cross-validation method

Prediction analysis was performed using single-cell values from all cells, as well as after selecting a sub-population of cells most affected by inhibitor treatment. A neural network previously described for cell morphological data[34] was used to conduct the experiments. The input was tabular data containing single-cell values, and the outputs were classification accuracy scores, presented as percentages. To validate the accuracy, we utilised 10-fold cross-validation, which split the dataset into 10 random folds while preserving the percentage of samples in each class across all folds. Each fold was used as a test set (10% of the data), with the remaining folds (90%) serving as the training and validation sets. The model was run and tested on each fold, resulting in 10 evaluated accuracies, which were then averaged to calculate the mean accuracy. The R script file is available as Supplementary File. 6.

Data availability

Data is provided within the manuscript or supplementary information files.

Received: 17 October 2024; Accepted: 24 April 2025
Published online: 14 May 2025

References

1. Wali, G. et al. Pharmacological rescue of mitochondrial and neuronal defects in SPG7 hereditary spastic paraplegia patient neurons using high throughput assays. *Front. NeuroSci.* **17** https://doi.org/10.3389/fnins.2023.1231584 (2023).
2. Cid-Castro, C., Hernández-Espinosa, D. R. & Morán, J. ROS as regulators of mitochondrial dynamics in neurons. *Cell. Mol. Neurobiol.* **38**, 995–1007. https://doi.org/10.1007/s10571-018-0584-7 (2018).
3. Duarte, F. V., Ciampi, D. & Duarte, C. B. Mitochondria as central hubs in synaptic modulation. *Cell. Mol. Life Sci.* **80**, 173. https://doi.org/10.1007/s00018-023-04814-8 (2023).
4. Quintana-Cabrera, R. & Scorrano, L. Determinants and outcomes of mitochondrial dynamics. *Mol. Cell.* **83**, 857–876. https://doi.org/10.1016/j.molcel.2023.02.012 (2023).
5. Chen, L. et al. Mitochondrial heterogeneity in diseases. *Signal. Transduct. Target. Ther.* **8**, 311. https://doi.org/10.1038/s41392-023-01546-w (2023).
6. Eisner, V., Picard, M. & Hajnóczky, G. Mitochondrial dynamics in adaptive and maladaptive cellular stress responses. *Nat. Cell. Biol.* **20**, 755–765. https://doi.org/10.1038/s41556-018-0133-0 (2018).
7. Arnold, B., Cassady, S. J., VanLaar, V. S. & Berman, S. B. Integrating multiple aspects of mitochondrial dynamics in neurons: age-related differences and dynamic changes in a chronic rotenone model. *Neurobiol. Dis.* **41**, 189–200. https://doi.org/10.1016/j.nbd.2010.09.006 (2011).
8. Koopman, W. J. H., Visch, H. J., Smeitink, J. A. M. & Willems, P. H. G. M. Simultaneous quantitative measurement and automated analysis of mitochondrial morphology, mass, potential, and motility in living human skin fibroblasts. *Cytometry Part. A.* **69A**, 1–12. https://doi.org/10.1002/cyto.a.20198 (2006).
9. Toyama, E. Q. et al. AMP-activated protein kinase mediates mitochondrial fission in response to energy stress. *Science* **351**, 275–281. https://doi.org/10.1126/science.aab4138 (2016).
10. Bray, M. A. et al. Cell painting, a high-content image-based assay for morphological profiling using multiplexed fluorescent dyes. *Nat. Protoc.* **11**, 1757–1774. https://doi.org/10.1038/nprot.2016.105 (2016).
11. Chandrasekaran, S. N., Ceulemans, H., Boyd, J. D. & Carpenter, A. E. Image-based profiling for drug discovery: due for a machine-learning upgrade? *Nat. Rev. Drug Discovery.* **20**, 145–159. https://doi.org/10.1038/s41573-020-00117-w (2021).
12. Pahl, A. et al. Morphological subprofile analysis for bioactivity annotation of small molecules. *Cell. Chem. Biology.* **30**, 839–853e837. https://doi.org/10.1016/j.chembiol.2023.06.003 (2023).
13. Way, G. P. et al. Morphology and gene expression profiling provide complementary information for mapping cell state. *Cell. Syst.* **13**, 911–923e919. https://doi.org/10.1016/j.cels.2022.10.001 (2022).
14. Ziegler, S., Sievers, S. & Waldmann, H. Morphological profiling of small molecules. *Cell. Chem. Biology.* **28**, 300–319. https://doi.org/10.1016/j.chembiol.2021.02.012 (2021).
15. Wali, G., Berkovsky, S., Whiten, D. R., Mackay-Sim, A. & Sue, C. M. Single cell morphology distinguishes genotype and drug effect in hereditary spastic paraplegia. *Sci. Rep.* **11**, 16635. https://doi.org/10.1038/s41598-021-95995-4 (2021).
16. Marklein, R. A. et al. Morphological profiling using machine learning reveals emergent subpopulations of interferon-γ–stimulated mesenchymal stromal cells that predict immunosuppression. *Cytotherapy* **21**, 17–31. https://doi.org/10.1016/j.jcyt.2018.10.008 (2019).
17. Becht, E. et al. Dimensionality reduction for visualizing single-cell data using UMAP. *Nat. Biotechnol.* **37**, 38–44. https://doi.org/10.1038/nbt.4314 (2019).
18. van der Stel, W. et al. High-content high-throughput imaging reveals distinct connections between mitochondrial morphology and functionality for OXPHOS complex I, III, and V inhibitors. *Cell Biol. Toxicol.* **39**, 415–433. https://doi.org/10.1007/s10565-022-09712-6 (2023).
19. Little, D. et al. A single cell high content assay detects mitochondrial dysfunction in iPSC-derived neurons with mutations in <i>snca. *Sci. Rep.* **8** https://doi.org/10.1038/s41598-018-27058-0 (2018).
20. Willems, P. H. G. M., Rossignol, R., Dieteren, C. E. J., Murphy, M. P. & Koopman, W. J. H. Redox homeostasis and mitochondrial dynamics. *Cell Metabol.* **22**, 207–218. https://doi.org/10.1016/j.cmet.2015.06.006 (2015).
21. Bulthuis, E. P., Adjobo-Hermans, M. J. W., Willems, P. & Koopman, W. J. H. Mitochondrial morphofunction in mammalian cells. *Antioxid. Redox. Signal.* **30**, 2066–2109. https://doi.org/10.1089/ars.2018.7534 (2019).
22. Benard, G. et al. Mitochondrial bioenergetics and structural network organization. *J. Cell Sci.* **120**, 838–848. https://doi.org/10.1242/jcs.03381 (2007).
23. Glancy, B., Kim, Y., Katti, P. & Willingham, T. B. The functional impact of mitochondrial structure across subcellular scales. *Front. Physiol.* **11**, 541040. https://doi.org/10.3389/fphys.2020.541040 (2020).
24. Shah, S. I., Paine, J. G., Perez, C. & Ullah, G. Mitochondrial fragmentation and network architecture in degenerative diseases. *PLoS One.* **14**, e0223014. https://doi.org/10.1371/journal.pone.0223014 (2019).
25. Mannella, C. A., Lederer, W. J. & Jafri, M. S. The connection between inner membrane topology and mitochondrial function. *J. Mol. Cell. Cardiol.* **62**, 51–57. https://doi.org/10.1016/j.yjmcc.2013.05.001 (2013).
26. Cogliati, S., Enriquez, J. A. & Scorrano, L. Mitochondrial Cristae: where beauty Meets functionality. *Trends Biochem. Sci.* **41**, 261–273. https://doi.org/10.1016/j.tibs.2016.01.001 (2016).

27. Gilkerson, R. W., Selker, J. M. L. & Capaldi, R. A. The cristal membrane of mitochondria is the principal site of oxidative phosphorylation. *FEBS Lett.* **546**, 355–358. https://doi.org/10.1016/S0014-5793(03)00633-1 (2003).
28. Tasseva, G. et al. Phosphatidylethanolamine deficiency in mammalian mitochondria impairs oxidative phosphorylation and alters mitochondrial Morphology *. *J. Biol. Chem.* **288**, 4158–4173. https://doi.org/10.1074/jbc.M112.434183 (2013).
29. Gottlieb, E., Armour, S. M., Harris, M. H. & Thompson, C. B. Mitochondrial membrane potential regulates matrix configuration and cytochrome C release during apoptosis. *Cell. Death Differ.* **10**, 709–717. https://doi.org/10.1038/sj.cdd.4401231 (2003).
30. Westrate, L. M., Drocco, J. A., Martin, K. R., Hlavacek, W. S. & MacKeigan, J. P. Mitochondrial morphological features are associated with fission and fusion events. *PLoS One.* **9**, e95265. https://doi.org/10.1371/journal.pone.0095265 (2014).
31. Charrasse, S. et al. Quantitative assessment of mitochondrial morphology relevant for studies on cellular health and environmental toxicity. *Comput. Struct. Biotechnol. J.* **21**, 5609–5619. https://doi.org/10.1016/j.csbj.2023.11.015 (2023).
32. Charrasse, S. et al. Quantitative imaging and semiotic phenotyping of mitochondrial network morphology in live human cells. *PLoS One.* **19**, e0301372. https://doi.org/10.1371/journal.pone.0301372 (2024).
33. Wang, V. et al. Attenuating mitochondrial dysfunction and morphological disruption with PT320 delays dopamine degeneration in mitopark mice. *J. Biomed. Sci.* **31** https://doi.org/10.1186/s12929-024-01025-6 (2024).
34. D'Sa, K. et al. Prediction of mechanistic subtypes of Parkinson's using patient-derived stem cell models. *Nat. Mach. Intell.* **5**, 933–946. https://doi.org/10.1038/s42256-023-00702-9 (2023).
35. Gantner, C. W. et al. FGF-MAPK signaling regulates human deep-layer corticogenesis. *Stem Cell. Rep.* **16**, 1262–1275. https://doi.org/10.1016/j.stemcr.2021.03.014 (2021).
36. Leone, D. P., Srinivasan, K., Chen, B., Alcamo, E. & McConnell, S. K. The determination of projection neuron identity in the developing cerebral cortex. *Curr. Opin. Neurobiol.* **18**, 28–35. https://doi.org/10.1016/j.conb.2008.05.006 (2008).
37. Wali, G. et al. Generation of human-induced pluripotent-stem-cell-derived cortical neurons for high-throughput imaging of neurite morphology and neuron maturation. *STAR. Protocols.* **4**, 102325. https://doi.org/10.1016/j.xpro.2023.102325 (2023).
38. Bucevičius, J., Lukinavičius, G. & Gerasimaitė, R. The use of Hoechst dyes for DNA staining and beyond. *Chemosensors* **6**, 18 (2018).
39. Castelo Rueda, M. P. et al. Molecular phenotypes of mitochondrial dysfunction in clinically non-manifesting heterozygous PRKN variant carriers. *NPJ Parkinsons Dis.* **9** https://doi.org/10.1038/s41531-023-00499-9 (2023).
40. Wickham, H. *ggplot2: Elegant Graphics for Data Analysis* (Springer-, 2016).
41. Slowikowski, K. *ggrepel: Automatically Position Non-Overlapping Text Labels with 'ggplot2'*, (2024). https://ggrepel.slowkow.com/, https://github.com/slowkow/ggrepel
42. Ritchie, K. U. a. J. A. a. H. W. a. G. *rstudioapi: Safely Access the RStudio API*, (2022). https://rstudio.github.io/rstudioapi/, https://github.com/rstudio/rstudioapi
43. Ashhurst, T. M. et al. Integration, exploration, and analysis of high-dimensional single-cell cytometry data using spectre. *Cytometry Part. A.* **101**, 237–253. https://doi.org/10.1002/cyto.a.24350 (2022).
44. Garnier, S., Ross, Noam, R. & Pedro, C. A. Sciaini, Marco, Scherer, Cédric. *viridis(Lite)} - Colorblind-Friendly Color Maps for R*, < (2024). https://sjmgarnier.github.io/viridis/
45. Kassambara, A. *ggpubr: 'ggplot2' Based Publication Ready Plots*, < (2023). https://rpkgs.datanovia.com/ggpubr/
46. Milošević, D. et al. The application of uniform manifold approximation and projection (UMAP) for unconstrained ordination and classification of biological indicators in aquatic ecology. *Sci. Total Environ.* **815**, 152365. https://doi.org/10.1016/j.scitotenv.2021.152365 (2022).
47. Mächler, M., Rousseeuw, P., Struyf, A., Hubert, M. & Hornik, K. *Cluster: Cluster Analysis Basics and Extensions*. Vol. 1 (2012).
48. Venables, B. & Ripley, B. (2002).
49. Wilke, C. O. *cowplot: Streamlined Plot Theme and Plot Annotations for 'ggplot2'*, (2024). https://wilkelab.org/cowplot/

Acknowledgements

This work was supported by the "Rising star" grant award to GW from by Neuroscience Research Australia (NeuRA), Australia. We would like to thank Professor Marie Dziadek for her critical review of the manuscript and constructive feedback that helped improve the overall quality of the paper. We thank Thomas Ashhurst, Sydney Cytometry Core Research Facility, University of Sydney for his advice on single-cell data analysis using the Spectre R-studio analysis package. The imaging component of this study was carried out using instruments situated in, and maintained by, the Katharina Gaus Light Microscopy Facility (KGLMF) at UNSW.

Author contributions

G.W., R.S., and C.M.S. conceived and designed the experiments. M.B.H., Y.L and G.W. performed the cell culture experiments. H.P. and G.W. provided detailed descriptions of the image morphological features used in this study. G.W. performed the image data extraction and visualisation for group and single cell analysis. R.S, G.W., and H.X., performed the statistical analysis. R.S, G.W., prepared the first manuscript draft. All authors contributed to and edited the paper. G.W. and C.S. provided funding for the research.

Declarations

Competing interests

The authors declare no competing interests.

Additional information

Supplementary Information The online version contains supplementary material available at https://doi.org/10.1038/s41598-025-99972-z.

Correspondence and requests for materials should be addressed to G.W.